# Effects of alloying addition on deformation mechanisms, microstructure, texture and mechanical properties in Fe-12Mn-0.5C austenitic steel

Rajib Kalsar, Ranjit Kumar Ray, Satyam Suwas

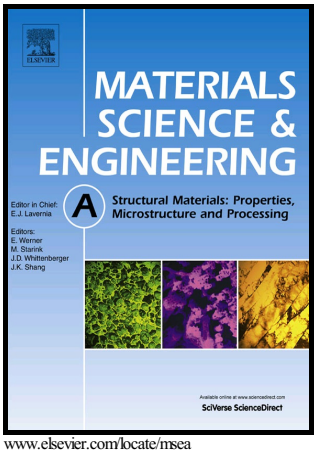


www.elsevier.com/locate/msea

PII: S0921-5093(18)30730-5
DOI: https://doi.org/10.1016/j.msea.2018.05.071
Reference: MSA36509

To appear in: *Materials Science & Engineering A*

Received date: 15 August 2017
Revised date: 30 March 2018
Accepted date: 19 May 2018

Cite this article as: Rajib Kalsar, Ranjit Kumar Ray and Satyam Suwas, Effects of alloying addition on deformation mechanisms, microstructure, texture and mechanical properties in Fe-12Mn-0.5C austenitic steel, *Materials Science & Engineering A,* https://doi.org/10.1016/j.msea.2018.05.071

# Effects of alloying addition on deformation mechanisms, microstructure, texture and mechanical properties in Fe-12Mn-0.5C austenitic steel

Rajib Kalsar[a], Ranjit Kumar Ray[b] and Satyam Suwas[a*]

[a]Department of Materials Engineering, Indian Institute of Science, Bangalore-560012, India.

[b]M N Dastur Centre for Materials Science and Engineering, Indian Institute of Engineering Science and Technology, Shibpur-711103, India

***Corresponding author: satyamsuwas@iisc.ac.in**



## Abstract

In the present investigation, the dependence of deformation mechanisms on quaternary alloying addition has been investigated for medium Mn austenitic steel. A steel with composition Fe-12Mn-0.5C-X (X: Ni and Al), a medium Mn austenite steel was deformed up to 60% by cold reduction to investigate the deformation mechanisms and texture evolution. Electron Back-scattered Diffraction (EBSD) and X-ray bulk texture measurement have been performed to study the deformation behaviour. Deformed microstructure with increasing strain was systematically analyzed with respect to the alloying addition. SFE of the alloy can be tailored by the addition of alloying elements. In the present investigation, SFE has been tailored by addition of Carbon, Aluminium and Nickel. The highest deformation twin fraction has been observed in Ni added sample and the lowest in the Al-added sample. Visco plastic self-consistent (VPSC) simulation has been performed to understand the contribution of slip and twin activity during deformation.

**Keywords:** TWIP steel, texture, microstructure, twin, VPSC, mechanical properties

## 1. Introduction

Twinning induced plasticity (TWIP) and transformation induced plasticity (TRIP) steels possess excellent combinations of specific strength and ductility [1-4]. Due to these attributes the crash resistance or energy absorption is much higher for such steels, and this makes these materials good candidates for automotive applications [5]. TWIP steels have an austenitic structure and contain quite high amounts of Manganese (Mn). Addition of Mn to steel brings down its stacking fault energy (SFE) to a large extent and, therefore, high Mn TWIP steels possess low SFE. The SFE of these steels can be further tailored by adding alloying elements, such as C, Al, Ni, Si, N etc. Addition of C increases SFE even further and favours the TWIP effect in high Mn steels [6]. DeCooman et al. [7] and Jin et al. [8] reported that in a Fe-18Mn-0.6C TWIP steel, having a SFE of 13 $mJ/m^2$, with addition of every 1 wt% Al the SFE increases by approximately +11.3 $mJ/m^2$ and +7.8 $mJ/m^2$, respectively. Addition of Al also helps in retarding the formation of cementite precipitates [8, 9], in increasing the yield strength by solid solution strengthening [1] and in resisting hydrogen embrittlement in Mn steels [10]. Ni addition to TWIP steels has not been studied to any great extent, however, it is a commonly used element in austenitic stainless steels and for stabilizing the austenite phase [11, 12].

Stacking fault energy is known to play an important role in deciding the deformation mechanisms in FCC materials, and also in the development of microstructure and texture and in the evolution of mechanical properties [13, 14]. It is now known that in materials having SFE in the range 18-35 $mJm^{-2}$, deformation takes place by twinning while for SFE values lesser than this deformation occurs by twinning as well as by strain-induced martensitic transformation (SIMT), the latter being the predominant process [13, 15]. Remy and Pineau [14] reported that the minimum SFE required for mechanical twinning is 9 mJ $m^{-2}$, while ε -martensite can form when SFE < 12 $mJm^{-2}$.

Texture evolution in FCC materials is well established with respect to SFE. Two types of textures generally form in FCC materials, (i) Cu-type texture, formed in high to medium SFE materials such as Al, Cu, Ni etc, and comprising the Cu {112} behaviour <111>, S {123} <634> and Bs {110} <112> components [16]; and (ii) α-brass type texture, formed in low SFE materials, such as α-Brass, Ag, austenitic steels, Ni-60Co alloy and comprising predominantly the Bs {110} <112> and the Goss {110}<001> components [17-19]. Cu-type texture is produced when deformation takes place mainly by slip and in materials where cross slip is an easier process [20]. In low SFE materials, brass-type texture is generally formed where deformation is dominated by twinning and where cross slip is difficult [21, 22]. It has also been reported that twinning may not be sufficient as a deformation mode for the formation of brass -type texture, and that macroscopic shear bands and extended latent hardening could also be responsible for the development of this type of texture [23, 24].

The high strain hardening rate in TWIP steels has been known to be due to the presence of very high fractions of deformation twins and the interaction between them [25, 26]. The twin boundaries are act as obstacles to the motion of dislocations thereby increasing the amount of strain hardening. The fine lamellar mechanical twins, forming rapidly, keep on sub-dividing the original grains and this decreases the mean free path for dislocation motion, which causes further enhancement of strain hardening. Hardening due to twinning, known as dynamic Hall-Petch effect, has been reported in many FCC materials containing very high volume fractions of deformation twins [27, 28]. Mn and C in high Mn TWIP steels are reported to give rise to local ordering or clustering, which further enhances strain hardening [29]. DeCooman et al. [29] reported dynamic strain aging (DSA) in TWIP steels at room temperature due to solute C atom placed in octahedral void positions. The clusters of Mn-C can become much more effective obstacle for dislocation movement than Mn and C atoms alone. Chen et al.[30] reported that dynamic strain aging in TWIP steels is due to interaction between Mn-C clusters (or dipoles) and dislocations.

In the present investigation, an attempt has been made to reduce the Mn content and to substitute it by some other suitable elements to get TWIP effects. A medium Mn TWIP steel, along with its two variations obtained by addition of Al and Ni to the base composition, have been studied and the effects of alloying addition on the deformation mechanisms, microstructural and texture evolution as well as on mechanical properties have been examined. Even though high Mn TWIP steels have excellent combination of mechanical properties (strength and ductility), these materials are not in use yet because of limitations, related to melting of steels with high Mn, homogenisation, delayed cracking etc. It would be worthwhile to investigate if all these drawbacks could be overcome by reducing the Mn content and or by substituting Mn by some other elements.

## 2. Experimental Procedure

### 2.1 Materials and Processing

The materials used in this experiment were three Fe-12Mn-0.5C-nX (X=Ni and Al) steels (Table 1), which were melted in an arc melting furnace under argon atmosphere. The charges were melted several times to get homogeneous compositions. The button shaped samples were homogenized in a high vacuum furnace ($<10^{-5}$ mbar) at 1000°C for 5 hrs. The homogenized samples were cross rolled up to 50 % and then recrystallized at 800°C for 30 minutes, resulting in an equiaxed grain shape and weak texture. These materials were treated as the starting materials for further study. These were unidirectionally cold rolled down to 20%, 40% and 60% reduction in thickness (Table 2).

### 2.2 Characterizations

#### 2.2.1 Structural and Microstructural Characterization

Structural investigation was carried out using X-ray diffraction (XRD) with Cu Kα (λ~1.54404 Å) radiation and operated at 40 kV and 40 mA. The scanning range and step size were 40°-100° and 0.02° respectively for all samples. The samples were electro-polished before XRD scan to remove the strain induced martensite formed during earlier stages of polishing.

Microstructural characterization of the cold rolled samples was carried out in a field emission scanning electron microscope (FE-SEM), using an FEI Sirion model microscope and equipped with an Electron Backscatter Diffraction (EBSD) system. The SEM was operated at 25kV and the step size for scanning in EBSD was kept at 200 nm for all the samples. EBSD scans were performed on the transverse planes (TD direction) of rolled samples. Rolled samples for EBSD were first mechanically polished on wet SiC-paper (400-3000 grit) followed by electro-polishing, using Struers LectroPol 5 at ~5°C in 5% perchloric acid , at a polishing voltage of 26 V. Data acquisition and analyses were carried out using TSL-OIM software version 5.2.

### 2.2.2 Crystallographic Texture

Bulk texture measurements on the rolled samples were carried out using an X-ray texture goniometer (D8 Discover, Bruker AXS, Germany) having Schulz reflection geometry and with CuKα radiation. Four incomplete pole figures (α = 0-75°) from (111), (200), (220) and (311) peaks were measured at the mid-thickness sections parallel to the rolling plane. The three-dimensional orientation distribution functions (ODF) were calculated from the measured pole figures, using Mtex$^{(R)}$ (Matlab based tool) [31]. Orthotropic sample symmetry was imposed on the rolled samples for the purpose of texture representation. The Miller indices and the corresponding Euler angles of a few such components are given in Table 3.The locations of some important texture fibres in the orientation space and the Euler angles for the start and end points of the fibres are indicated in Table 4.

### 2.2.3 Mechanical Properties

The rolled samples were annealed at 800°C for 30 minutes to get complete recrystallized state. Flat dog-bone shaped tensile specimen was cut out from the rolled annealed sheet. The gauge length is parallel to the rolling direction (RD) and width is parallel to the transverse direction (TD). The gauge length was 6 mm, width 2 mm and thickness ~ 0.6 mm. The uniaxial tensile tests were carried out in Instron Servo-hydraulic UTM. Tensile tests were performed at room temperature and the strain rate was kept at $10^{-3}$ $sec^{-1}$.

### 3. Visco-plastic self consistent (VPSC) simulation



In order to understand the contribution of different microscopic deformation mechanisms (slip and twin) responsible for the evolution of observed rolling textures in the three steels, texture simulation was performed using the Visco-plastic self consistent (VPSC) model. The use of the VPSC model to simulate the deformation texture at large strains and strain rates was first proposed by Molinari [32], and was further extended by Lebensohn and Tome´[33] to account for anisotropic deformation behavior in polycrystalline materials. In the VPSC model, each grain is treated as an ellipsoidal inclusion embedded within a homogeneous equivalent medium (HEM) and the velocity and velocity gradient of each medium (grain and matrix) is considered different during deformation.

In this model, the interaction between each individual grain and the HEM is taken into account, using the Eshelby inclusion formalism. The model predicts both the macroscopic stress–strain response and microscopic slip and twin activities with incremental stress and strain rate. In the self-consistent approach, the strain rate $\dot{\varepsilon}_{ij}$ in a grain is related to the grain stress σ by the following constitutive equation:

$$\dot{\boldsymbol{\varepsilon}}_{\mathbf{ij}}^{\mathbf{c}} = \dot{\boldsymbol{\gamma}}_{\mathbf{0}} \sum_{\mathbf{s}} \mathbf{m}_{\mathbf{ij}}^{\mathbf{s}} \left[\frac{\mathbf{m}_{\mathbf{kl}}^{\mathbf{s}} \boldsymbol{\sigma}_{\mathbf{kl}}}{\boldsymbol{\tau}^{\mathbf{s}}}\right]^{\mathbf{n}} \qquad (1)$$

Here, s refers to the slip/twin system; $\tau^s$ is the threshold stress (critical resolved shear stress (CRSS)); n is the inverse of strain-rate sensitivity; $\dot{\gamma}_0$ is the reference strain rate; $m_{ij}^s$ is the symmetric Schmid tensor given by $\frac{1}{2}(b_i^s n_j^s + b_j^s n_i^s)$, where b is the Burgers vector, n is the slip plane normal. The term $m_{kl}^s \sigma_{kl}$ represents the resolved shear stress acting on slip and twinning systems, which evolves as a function of deformation. The evolution of resolved shear stress on any slip system s as a function of deformation is given by the empirical extended Voce hardening law [34]:

$$\boldsymbol{\tau}^{\mathbf{s}} = \boldsymbol{\tau}_{\mathbf{0}}^{\mathbf{s}} + (\boldsymbol{\tau}_{\mathbf{1}}^{\mathbf{s}} + \boldsymbol{\theta}_{\mathbf{1}}^{\mathbf{s}} \Gamma)\left(\mathbf{1} - \mathbf{exp}\left(-\Gamma \left|\frac{\boldsymbol{\theta}_{\mathbf{0}}^{\mathbf{s}}}{\boldsymbol{\tau}_{\mathbf{1}}^{\mathbf{s}}}\right|\right)\right) \qquad (2)$$

where, $\tau_0^s$ is the initial CRSS, $\theta_0^s$ ,$\theta_1^s$ are initial and asymptotic hardening rate during deformation, $\tau_1^s$ is the back extrapolated threshold stress, $\Gamma = \int_0^t \Delta\dot{\gamma}^s$ gives the accumulated shear strain. The Voce hardening parameters were identified from experimental stress-strain curves to simulate the deformation texture.

The VPSC model is based on solving local stress equilibrium equations for an ellipsoidal inclusion embedded in a matrix (homogenous effective medium). The matrix-grain interaction equation can be written as:

$$M^c = n^{eff}(I - E)^{-1} \quad (3)$$

where M is the interaction tensor, E is the Eshelby tensor and I is the identity matrix. $n^{eff}$ is a variable which dictates the strength of interaction between grain-matrix. In this model, various homogenization schemes (e.g. secant, tangent, affine, $n^{eff}$ approaches) can be incorporated to account for the grain interaction [35]. Based on the $n^{eff}$ value, the self-consistent approach follows different types of model: (i) $n^{eff}$=1, for the secant scheme, which tends to the Taylor-type model (uniform stress state), (ii) $n^{eff}$=20, for tangent scheme, which tends to the Sachs-type model (uniform-strain state), (iii) $n^{eff}$=10, follows an intermediate type interaction between the secant and tangent schemes. In order to account for the volume effect of reoriented twins in texture evolution, Predominant Twin Reorientation (PTR) model has also been incorporated in the scheme of things [36]. In the PTR model, grains are reoriented towards the highest twin system, when the twin fraction exceeds threshold value. This model has been successfully used to predict texture evolution in twinning systems, for example, in silver during Equal Chanel Angular Extrusion [37]. Recently, Saleh et al. [38] and Beyerlien et al. [39] also used the PTR scheme in VPSC modelling to incorporate the twinning volume effect in TWIP steels and Ag-Cu alloys, respectively.

## 4. Results

### 4.1 Structural evolution

Fig. 1 show the XRD plots (2θ vs. intensity) for the steels-1, 2 and 3 for the deformation levels corresponding to thickness reductions 20%, 40% and 60%, respectively. The initial materials for all the three compositions consist of a fully austenitic structure. No evidence of the presence of

martensite was observed in any of the initial materials. Very small fraction of strain induced α'-martensite was detected in steel-2 at 40% and in steel-1 at 60% reduction levels (Fig. 1c and d). No strain induced martensitic phase transformation has been observed in steel-3 (Ni-added sample).

**4.2 Texture evolution**

The (111) pole figures for the three starting materials show that the initial textures in all three of them are rather weak and similar, consisting of the γ-fibre (Fig. 2). The $\Phi_2$ = 0°, 45° and 65° sections of the ODFs for all the three 40% and 60% cold rolled steels are shown in Fig. 3a and b. The ODF sections after 40% reduction indicate that the deformation texture is reasonably well-formed at this stage. All the three steels show a texture comprising of a moderate cube fiber and a well-developed alpha fiber, centered on the Goss orientation, which extends over the Brass (Bs) orientation. The Cu orientation in all the three steels is of rather weak intensity, while a weak S orientation can be seen in the ODF section for steel-2 only. Textures of steel 1 and 3 are quite similar in the sense that shows a moderate gamma fiber, although the Goss component exhibits slightly higher intensity in steel-3 than in steel-1. Steel-2, on the other hand shows the strongest intensity for the Goss compared to the other two and a perceptible peak at the Bs location. Steel-2 does not show any gamma fibre, which is, however present in the texture of the other two steels. Overall, the deformation textures formed in the three steels may be described as α-brass or alloy type, which is typical of low SFE alloys. After 60% cold rolling all the three steels show similar deformation textures in the sense that all of them show a moderate cube fibre, a reasonably strong α-fibre, centred on the Goss location, along with a moderate γ-fibre. The intensity of the Goss orientation at this stage is the highest for steel-3 (Fig. 3b). There is no noticeable change in the overall texture intensity in the 60% deformed materials, as compared to the 40% deformed materials.

A comparative study of textural evolution in the three steels, as a function of the amount of cold deformation, can be had from the fibre plots which connect different ideal texture

components in the Euler space and also indicate the quantitative variations of texture intensities (f ($g$)) with strain. Figs. 4 and 5 show the fibre plots for all the three steels, cold-rolled by an amount of 40% and 60%, respectively. Here the α-fibre consists of orientations with <110> ‖ ND and this fibre is observed in the $\Phi_2 = 0°$ section with $\Phi = 45°$ and $\Phi_1$ extending from 0° to 90°. It is clear that the f ($g$) values for Goss ($\Phi_1 = 0°$) and Bs ($\Phi_1 = 35°$) components increase steadily with alloying addition (that is with Al and Ni). The β-fibre is the one which connects the Cu, S and Bs orientations across different $\Phi_2$ sections.

The β-fibre plots clearly show the maximum intensity at the Bs position and the minimum at the Cu location, for all the three steels, for both the levels of deformation. A weak S orientation is clearly visible in all these plots. The course of the β-fibres unambiguously shows that all the three steels exhibit a clear alpha-brass or alloy type deformation texture, characteristic of low SFE materials. The τ-fibre consists of orientations with <1 1 0> || TD and is situated in the $\Phi_2 = 45°$ section at $\Phi_1 = 90°$ and extends from $\Phi = 0°$ to 90°. The plots of the τ-fibre show maxima at the Goss, Cu and at a location, midway between the Cu and Cu-T orientations. There is a noticeable intensity at the Cu-T position also. After 60% cold deformation, steel-3 shows the highest values of f (g) at the Goss and Cu-T locations. Overall, there is only a marginal decrease of f (g) with increasing cold deformation in steel-1 and 3, a very substantial difference observed in steel-2.

### 4.3 Texture simulation

An intermediate, "$n^{eff} = 10$" homogenization scheme has been used to simulate the rolling texture of all the alloys. The input texture of 2000 single orientations, for the simulations, was obtained by discretizing the ODF of the starting material [40]. The deformation imposed is considered to be plane-strain compression (compression along ND and elongation along RD), and the parameters $\tau_0^s$, $\tau_1^s$, $\theta_0^s$ and $\theta_1^s$ used for the slip and twin systems are listed in Table 5 for the three steels. The 12 octahedral slip ({111} <110>) and the 12 twin ({111} <112>) systems have been incorporated in the simulation. The goodness of the simulation was decided based on the qualitative similarity between the experimental and simulated ODFs (Figs. 3 and 6). The

simulated textures match qualitatively with the experimental textures, though the intensities of simulated textures are much higher. Figs. 7a and b shows the contributions of the slip and twin activity and twin volume fraction to the evolution of the simulated final textures for the three steels.

### 4.4 Microstructural evolution

In order to follow the microstructural evolution in the three steels, as a function of cold rolling, EBSD was performed on the transverse planes of the different samples. Fig. 8 shows the initial microstructures of steels 1 to 3. The grains in all the steels 1-3 are nearly equiaxed in shape with average grain size 25 μm, 50 μm and 45 μm, respectively. All the three microstructures show the presence of a few short and straight annealing twins; steel-3 (with Ni addition) seems to possess a higher annealing twin fraction than steel-1, while steel-2 (with Al addition) hardly shows any twin.

The microstructures of the 20% cold rolled steel samples are shown in Fig. 9. The presence of lenticular deformation twins is visible in all the microstructures; the deformation twin fraction being higher in case of steel-3 as compared to the other two steels. Usually the twins appear as bundles of micro-twins, the average thickness of an individual twin in the bundle is several nanometres only. The twins are formed parallel to one another, which is an indication of a single twin variant present within a grain.

Fig. 10 shows the microstructures of the 40% cold rolled steel samples. At this level of reduction, all the three steels reveal the presence of large fractions of deformation twins, indicating that twinning is the major active deformation mode at this stage. The highest twin fraction is observed again in steel-3 (Ni added) and the lowest in steel-2 (Al-added).

### 4.5 Mechanical properties

Fig. 11 depicting the true stress-true strain plots for steels 1 to 3, shows clearly that all of them exhibit good combination of strength and ductility. Among the three, the Ni added steel shows the

highest ductility and the lowest yield strength, while the Al added steel shows the lowest ductility and the highest yield strength. The actual values of UTS, YS and % elongation for all the three steels are shown in Table 6. In case of steel-1 (Al and Ni free), the strength, ductility and yield strength remain in between those of steels 2 and 3. The Fig. 11 clearly shows that the stress-strain curves for both the steels 1 and 3 are serrated, indicative of dynamic strain aging (DSA). This phenomenon is much more prominent in case of steel 3 than in steel 1. All the three experimental steels are seen to strain harden rapidly with strain.

## 5. Discussion

The stacking fault energy (SFE) of a metal or an alloy is considered as the most important parameter that influences the deformation behavior, microstructure, texture and strain-hardening response. In the present investigation, the SFE of a base TWIP steel composition was tailored by adding Ni and Al as alloying elements in a Fe-12Mn-0.5C alloy. Addition of Ni and Al in this alloy is known to decease and increases the SFE, respectively [7, 8, 12]. In the following subsections the precise roles of these alloying additions will be examined vis-à-vis their influence on the microstructural evolution during deformation, development of deformation texture and mechanical properties.

### 5.1 Microstructural evolution during deformation

The microstructural evolution in the three experimental steels during deformation is similar to those observed in (Fe-Ni-Cr) austenitic stainless steels [41] and in other low SFE materials, such as Ni-60Co alloys [42]. Deformation micro-twins appear in all the three steels right from the early stage of cold rolling (20% deformation).

The XRD plots (Fig. 1) clearly indicate that all the three steels are austenitic at room temperature and stable up to 60% cold rolling. The deformed microstructures of all the three steels very well show that the twin fraction at any stage of deformation is the highest for the Ni-added steel 3, while it is the lowest in the Al-added one (steel 2) (Figs. 9 and 10). The base steel (steel 1)

seems to possess a twin fraction lying in between these two. The twin boundary fraction plots for the three steels precisely depict the same (in Fig. 12). On the basis of the above results, it may be safely conjectured that the Ni-added steel 3 has the lowest and the Al-added steel 2 has the highest SFE among the three steels, with the base steel-1 having an intermediate value.

At low strains, deformation is expected to occur by contributions from both slip and twinning in all the steels. However, the relative weightages of the contributions will be different for the different steels, depending on their SFEs. This can also be found out from the misorientation angle plots for the three steels (Fig. 13). That deformation, even at an early stage, is highly slip dominated in the Al-added steel-2 than in the Ni-added steel-3, is manifested by the fact that the plot for the former shows a much higher fraction of low angle grain boundaries (LAGB) in the former than in the corresponding plot for the latter (Fig. 13b). Since the misorientation angle between a twin and its parent is about 60°, in FCC materials, a peak corresponding to 60° misorientation in the plot (Figs. 13a, b and c) points to the possibility of twin formation during deformation. 5° tolerance angle was used for twin boundary fraction calculation. A much higher value of the peak at 60° misorientation angle in the plot for steel 3, as compared to the steel 2, clearly indicates a higher volume fraction of twins, formed during deformation in the Ni-added steel 3, as compared to that in the Al-added steel 2. These differences between the two steels are qualitatively maintained at higher levels of deformation also (Fig. 13c). The simulation using VPSC model also predicts a higher twin activity in the Ni added steel and a rather low twin activity in the Al added steel (Fig. 7b). Some recent studies have indicated high twin activity in low to medium SFE Ni-Co alloys [42, 43], and in TWIP steel [19], at intermediate strain level.

In order to understand the distribution of intra-granular local misorientation and how it builds up with deformation, Kernel Average Misorientation (KAM) was measured and plotted in Fig. 14. This plot illustrates the average misorientation development between two neighbouring pixels within a deformed matrix. The misorientation with respect to the first nearest-neighbour

approximation is presented here. In all the steel samples, the KAM distribution shifts towards higher Kernel misorientation angles with increase in the amount of cold deformation. This indicates that the strain (caused by geometrically necessary dislocations) accumulates during deformation. In case of the Al added steel-2, the misorientation spread in KAM distribution is perceptibly more than in case of the Ni added steel-3. This clearly indicates that dislocation activity must be on a higher scale in the former than in the latter. As SFE is lower in case of steel-3 (Ni-added), the tendency of twin formation is more and the level of dislocation activity is less here, as compared to steel-2 (Al- added), which has a higher SFE.

At and above 60% reduction level, deformation takes place predominantly by the formation of macroscopic shear bands (SBs). Fig. 15 typically shows the distribution of shear bands throughout the steel-3. The other two alloys also show similar kind of shear band based deformation mode at this deformation level, which is a characteristic feature of low SFE materials [44]. It is well documented that macroscopic SBs are generally formed at ~ 35-45° angle with respect to the rolling direction (RD) in low SFE materials [45, 46], which is true in the present materials also.

**5.2 Development of deformation textures**

The very fact that the deformation textures of the three steels are not substantially different one from the other (Fig. 3), clearly indicates that the SFEs of the three steels are not significantly different. Of course, there are some subtle differences which may be attributed to some minor difference in their SFEs. All the steels were cold rolled to a maximum of 60% reduction. The deformation textures in all of them can be broadly described as being of the α-brass type, indicating that the SFEs in all of them can be considered to be on the lower side. The results have clearly shown that up to about 40% reduction, both slip and twinning are the important deformation modes, twinning being the predominant one in all the steels. However, the relative contributions of these two deformation modes in texture evolution are little different for the different steels. It is well known that in low SFE FCC materials, deformation twinning plays a

very significant role in texture evolution. The twin fraction decides the nature and strength of the final texture development up to certain amount of strain. The volume fraction of twins has two different effects in texture formation, (i) by way of changing the orientation of grains with respect to their parents, and (ii) by rapidly increasing the strain hardening by allowing twins to interact with other twins and also with dislocations. It has also been reported that deformation twins are not only responsible for brass-type texture evolution, in certain cases twinning also plays an important role to initiate formation of shear bands and extensive latent hardening, which is further responsible for causing deviation from Cu-type to brass-type texture [24]. In the present work, simulation has been carried out also up to 60% deformation. Because beyond 60% deformation, strain induced martensite and shear bands form, the present model cannot account for the shear bands formation and martensitic transformation during deformation. The experimentally calculated twin fraction (calculated from EBSD) and simulated twin fractions are in qualitative agreement (Fig. 12 and Fig. 7b). Using predominant twin re-orientation (PTR) model different twins volume fractions are incorporated in the three different steel samples. The highest fraction has been incorporated in steel-3 (Ni-added sample) and lowest in steel-2 (Al-added sample) which qualitatively matches with experimental twin fractions.

It has been already mentioned that addition of aluminium is supposed to increase the SFE and therefore should favour slip dominated deformation. However, this does not lead to any significant change in the deformation texture formed, although after 40% deformation the Al-added steel-2 shows the highest value of f(g) at both the Bs and Goss locations, as compared to the other two steels. On the other hand, after 60% deformation, the Ni-added steel 3 exhibits the highest f(g) values, among the three steels, at those locations. All the three steels, irrespective of the amount of deformation, invariably show higher texture intensity at the Goss location, as compared to the Bs. This has also been reported by Saleh et al. [47] for Fe-24Mn-3Al-2Si-1Ni-0.06C steel, and they ascribed it to large contributions from slip activity and micro shear banding. As expected, the f(g) values at Cu and S locations in Fig. 4b and Fig. 5b are very low indeed in all the steels at all deformation levels. The texture intensities at the Cu-T location are

also quite low and marginally different in all the three steels. This indicates that the twin volume effect may not contribute much towards texture evolution in these steels. It has been reported by many authors that twin volume fraction as such does not directly affect much in texture development in low SFE materials [48].

There may, however, be an indirect effect of twinning on texture evolution. It has been suggested that overshooting/latent hardening introduced by closely spaced twin lamellae on the primary slip plane can make the {111} planes approach an orientation parallel to the rolling plane. In fact, the intermediate development of the {111} texture components is considered essential for the occurrence of shear banding at later stages of deformation, leading to the development of brass-type texture in low SFE alloys [24]. It may be recalled here that after 40% deformation, both the steels-1 and 3 show weak {111} texture fibres, whereas the Al-added steel-2 does not show any such fibre (Fig. 4a). Steel-2 at this stage also shows the least twin fraction, among the three steels (Fig. 12). The extent of twinning and hence the degree of overshooting is less in steel-2, compared to the other two, and hence the γ-fibre may be suppressed. After further deformation up to 60%, however, all the three steels show weak {111} texture fibres as well as incidence of dense shear banding, which is in agreement with the suggestions of Leffers and Ray [24] for the formation of brass texture in low SFE materials.

### 5.3 Mechanical properties

There could be two different reasons for the high degree of strain hardening that has been achieved in all the three experimental Fe-12Mn-0.5C-nX alloys (Fig. 11). It has been reported that randomly distributed Mn and C in high Mn TWIP steels form a local order or clustering, where C sit in tetrahedral void position [29]. It has been reported that interactions between dislocations and Mn-C clusters give rise to strain hardening in Mn steels [29]. Dastur and Leslie [49] suggested that dislocations pinned by a Mn-C cluster due to the reorientation of cluster in a stress field near to dislocation core and causes pile-up of dislocations. However, the pinning force is not enough to stop the mobile dislocations fully. Therefore, the pinned dislocations released from cluster and propagate further, which causes DSA. In addition, Kim et al. [7] reported that C atoms interact

with dislocations and stacking faults (SFs) in TWIP steels. In a stacking fault (SF) region, the FCC stacking sequence locally changes to HCP, which will alter the environment of C atoms due the change in the positions of C atoms from octahedral to tetrahedral. This causes a local lattice distortion which could produce strengthening effect in TWIP steels [50]. The other important feature in the stress-strain plots are the serrations that have been observed in the curves for steel-1 and steel-3 (Fig. 11). The frequency of serration is much higher in steel-3 than in steel-1 and practically no serration or negligible serration has been observed in steel-2. The serrations in the stress-strain curves are characteristics of the dynamic strain aging (DSA) phenomenon [51]. DSA affects in strain hardening and increase the post uniform elongation significantly. It could very well be that a slower rate of formation of deformation twinning and a strong effect of Al atoms in remarkably reducing the activity and diffusivity of C atoms in steel-2 could be responsible for substantially or totally removing the DSA effect [52, 53].

Again, deformation twinning could also play a great role in strain hardening of these steels by interacting with dislocations. Twin volume fraction with increasing tensile deformation was calculated from VPSC simulation. Highest twin fraction was observed for steel-3 sample and lowest for steel-2 sample (Fig. 16). The uniform elongation and strain hardening is also shows similar trend, highest elongation was observed for steel-3 and lowest for steel-2 sample (Fig. 11). The twin boundaries are semi coherent and can act as obstacles to the motion of dislocations thereby increasing the amount of strain hardening. The rapid production of deformation twins with increasing strain will also ensure a higher rate of strain hardening [27, 54]. The fine lamellar mechanical twins, forming rapidly, keep on sub-dividing the original grains and this decreases the mean free path for dislocation motion, which causes further enhanced strain hardening [55]. Hardening due to twinning, known as dynamic Hall-Petch effect, has been reported in many FCC materials containing very high fractions of deformation twins [27, 28]. In fact, dynamic Hall-Petch phenomenon due to deformation twinning could be the reason for high amount and rate of strain-hardening in TWIP steels. The contribution of twins to the total flow stress can be incorporated in terms of the following Hall-Petch relationship:

$$\sigma = \sigma_0 + \frac{K_{H-P}}{(\lambda_{twin})^{1/2}} \quad \textbf{(5)}$$



where $\sigma_0$ is the friction stress, $K_{H-P}$ is the Hall-Petch constant and $\lambda_{twin}$ is the average twin thickness. However, thickness of twins, inter twin spacing and volume fractions of twins also play important roles in strain hardening [56].

## 6. Conclusions

The microstructure, texture and mechanical properties are systematically analyzed with respect to the effect of alloying addition and amount of deformation for three compositions of TWIP steel. The interpretation of experimental and simulation results lead to the following conclusions:

i. Up to a deformation corresponding to 60% rolling reduction austenitic phase is kinetically stable. Highest fraction of deformation twins has been observed in the Ni added sample.

ii. Up to 40% deformation, in the Al added sample; the fraction of Cu and S components is high which renders the texture to Cu-type. However, at 60% reduction level, texture is Bs-type. The Ni-added sample as well as the sample without Ni or Al added show Bs-type texture evolution throughout the deformation.

iii. Simulated textures agree well with the experimental textures. Variation in experimentally observed twin fraction and simulated twin fraction are in qualitative agreement. The simulations show highest twin activity in the Ni added sample and lowest in the Al added sample.

iv. Dynamic strain aging (DSA) is observed in the sample without Ni or Al and in the Ni added sample, not in Al-added sample. The extent of deformation twinning plays a major role in this phenomenon. Ni addition leads to a decrease in the yield strength and increase in elongation to failure, whereas Al addition shows an opposite effect.

**Acknowledgment**

Authors gratefully acknowledge Tata Steel India Ltd. for the financial support in the area of Mn Steels. We would like to thank Drs. Carlos Tome and Ricardo Lebensohn, Los Alamos National Laboratory, USA for providing the VPSC version 7b code. The extensive use of microscopes at the Advanced Facility of Microscopy and Microanalysis (AFMM) facility and XRD at the Institute X-ray facility, Indian Institute of Science (IISc), Bangalore is acknowledged.

**References**


1. De Cooman, B. O. Kwon, K. Chin, State-of-the-knowledge on TWIP steel, Mater. Sci. Technol., **28** (2012), pp. 513-527.
2. O. Bouaziz, S. Allain, C. P. Scott, P. Cugy, D. Barbier, High manganese austenitic twinning induced plasticity steels: A review of the microstructure properties relationships, Curr. Opin. Solid State Mater. Sci., **15** (2011), pp. 141-168.
3. O. Grässel, L. Krüger, G. Frommeyer, L.W. Meyer, High strength Fe–Mn–(Al, Si) TRIP/TWIP steels development-properties-application, Int. J. Plast., **16** (2000), pp. 1391-1409.
4. Y. F. Shen, Y. D. Liu, X. Sun, Y. D. Wang, L. Zuo, R. D. K. Misra, Improved ductility of a transformation-induced-plasticity steel by nanoscale austenite lamellae, Mater. Sci. Eng. A, **583 (**2013**)**, pp. 1-10.
5. R. Neu, Performance and characterization of TWIP steels for automotive applications, Mater. Perform. Charact., **2** (2013), pp. 244-284.
6. J. Nakano, P.J. Jacques, Effects of the thermodynamic parameters of the hcp phase on the stacking fault energy calculations in the Fe–Mn and Fe–Mn–C systems, Calphad, **34** (2010), pp. 167-175.
7. J. Kim, S.-J. Lee, B.C. De Cooman, Effect of Al on the stacking fault energy of Fe–18Mn–0.6C twinning-induced plasticity, Scr. Mater., **65** (2011), pp. 363-366.
8. J.-E. Jin, Y.-K. Lee, Effects of Al on microstructure and tensile properties of C-bearing high Mn TWIP steel, Acta Mater., **60** (2012), pp. 1680-1688.
9. S. Kang, Y.-S. Jung, J.-H. Jun, Y.-K. Lee, Effects of recrystallization annealing temperature on carbide precipitation, microstructure, and mechanical properties in Fe–18Mn–0.6 C–1.5 Al TWIP steel, Mater. Sci. Eng., A, **527** (2010), pp. 745-751.

10. M. Koyama, E. Akiyama, K. Tsuzaki, Hydrogen embrittlement in Al-added twinning-induced plasticity steels evaluated by tensile tests during hydrogen charging, ISIJ Int., **52** (2012), pp. 2283-2287.

11. L. Vitos, J.-O. Nilsson, B. Johansson, Alloying effects on the stacking fault energy in austenitic stainless steels from first-principles theory, Acta Mater., **54** (2006), pp. 3821-3826.

12. P. Ferreira, P. Müllner, A thermodynamic model for the stacking-fault energy, Acta Mater., **46** (1998), pp. 4479-4484.

13. S. Allain, J-P. Chateau, O. Bouaziz, S. Migot, N. Guelton, Correlations between the calculated stacking fault energy and the plasticity mechanisms in Fe–Mn–C alloys, Mat. Sci. Eng. A, **387 (**2004), pp. 158-162.

14. L. Remy, A. Pineau, Twinning and strain-induced FCC→ HCP transformation in the Fe-Mn-Cr-C system, Mater. Sci. Eng., **28** (1977), pp. 99-107.

15. L. Bracke, J. Penning, N. Akdut, The influence of Cr and N additions on the mechanical properties of FeMnC steels, Metall. Mater. Trans. A, **38** (2007), pp. 520-528.

16. R. Smallman, D. Green, The dependence of rolling texture on stacking fault energy, Acta Metall., **12** (1964), pp. 145-154.

17. R.K. Ray, Rolling textures of pure nickel, nickel-iron and nickel-cobalt alloys, Acta Metall. Mater., **43** (1995), pp. 3861-3872.

18. W. Heye, G. Wasserman, The formation of the rolling textures in fcc metals by slip and twinning, Scr. Metall., **2** (1968), pp. 205-207.

19. A.A. Saleh, C. Haase, E.V. Pereloma, D.A. Molodov, A.A. Gazder, On the evolution and modelling of brass-type texture in cold-rolled twinning-induced plasticity steel, Acta Mater., **70 (**2014**)**, pp. 259-271.

20. A. English, G. Chin, On the variation of wire texture with stacking fault energy in fcc metals and alloys, Acta metall., **13** (1965), pp. 1013-1016.

21. G. Wassermann, Der Einfluss Mechanischer Zwillingsbildung auf die Entstehung der Walztexturen Kubisch Flachenzentrierter Metalle, Z. Metallkunde, **54** (1963), pp. 61-65.

22. J. Hirsch, K. Lücke, M. Hatherly, Overview No. 76: Mechanism of deformation and development of rolling textures in polycrystalline fcc Metals-III. The influence of slip inhomogeneities and twinning, Acta Metall., **36** (1988), pp. 2905-2927.

23. A. Weidner, P. Klimanek, Shear banding and texture development in cold-rolled α-brass, Scr. Mater., **38** (1998), pp. 851-856.

24. T. Leffers, R.K. Ray, The brass-type texture and its deviation from the copper-type texture, Prog. Mater. Sci., **54** (2009), pp. 351-396.

25. O. Bouaziz, N. Guelton, Modelling of TWIP effect on work-hardening, Metall, Mater. Trans. A, **319 (**2001**)**, pp. 246-249.

26. D. Barbier, N. Gey, S. Allain, N. Bozzolo, M. Humbert, Analysis of the tensile behavior of a TWIP steel based on the texture and microstructure evolutions, Mat. Sci. Eng. A, **500** (2009), pp. 196-206.

27. O. Bouaziz, S. Allain, C. Scott, Effect of grain and twin boundaries on the hardening mechanisms of twinning-induced plasticity steels, Scr. Mater., **58** (2008), pp. 484-487.

28. S. Asgari, E. El-Danaf, S.R. Kalidindi, R.D. Doherty, Strain hardening regimes and microstructural evolution during large strain compression of low stacking fault energy fcc alloys that form deformation twins, Metall. Mater. Trans. A., **28** (1997), pp. 1781-1795.

29. S.-J. Lee, J. Kim, S. N. Kane, B.C. De Cooman, On the origin of dynamic strain aging in twinning-induced plasticity steels, Acta Mater., **59** (2011), pp. 6809-6819.

30. L. Chen, H.-S. Kim, S.-K. Kim, Localized deformation due to Portevin-LeChatelier effect in 18Mn-0.6 C TWIP austenitic steel, ISIJ Int., **47** (2007), pp. 1804-1812.

31. F. Bachmann, R. Hielscher, H. Schaeben, Texture analysis with MTEX–free and open source software toolbox, Solid State Phenom., **160 (**2010**)**, pp. 63-68.

32. A. Molinari, G. Canova, S. Ahzi, A self consistent approach of the large deformation polycrystal viscoplasticity, Acta Metall., **35** (1987), pp. 2983-2994.

33. R. Lebensohn, C. Tomé, A self-consistent anisotropic approach for the simulation of plastic deformation and texture development of polycrystals: application to zirconium alloys, Acta Metall. Mater., **41** (1993), pp. 2611-2624.

34. C. Tome, G.R. Canova, U.F. Kocks, N. Christodoulou, J.J. Jonas, The relation between macroscopic and microscopic strain hardening in FCC polycrystals, Acta Metall., **32** (1984), pp. 1637-1653.

35. R. Lebensohn, C. Tomé, Manual for code visco-plastic self-consistent (VPSC), version 7b, Los Alamos National Laboratory, 2007.

36. C. Tomé, R. Lebensohn, U. Kocks, A model for texture development dominated by deformation twinning: application to zirconium alloys, Acta Metall. Mater., **39** (1991), pp. 2667-2680.

37. I.J. Beyerlein, L.S. Tóth, C.N. Tomé, S. Suwas, Role of twinning on texture evolution of silver during equal channel angular extrusion, Philos. Mag., **87** (2007), pp. 885-906.

38. A.A. Saleh, E.V. Pereloma, A.A. Gazder, Microstructure and texture evolution in a twinning-induced-plasticity steel during uniaxial tension, Acta Mater., **61** (2013), pp. 2671-2691.

39. I.J. Beyerlein, N.A. Mara, D. Bhattacharyya, D.J. Alexander, C.T. Necker. Texture evolution via combined slip and deformation twinning in rolled silver–copper cast eutectic nanocomposite, Int. J. Plast., **27** (2011), pp. 121-146.

40. L.S. Toth, P. Van Houtte, Discretization techniques for orientation distribution functions, Textures Microstruct., **19** (1992), pp. 229-244.

41. M. Blicharski, S. Gorczyca, Structural inhomogeneity of deformed austenitic stainless steel, Met. Sci., **12** (1978), pp. 303-312.

42. R. Madhavan, R.K. Ray, S. Suwas, New insights into the development of microstructure and deformation texture in nickel–60wt.% cobalt alloy, Acta Mater., **78 (**2014**)**, pp. 222-235.

43. R. Madhavan, R.K. Ray, S. Suwas, Texture transition in cold-rolled nickel–40wt.% cobalt alloy, Acta Mater., **74 (**2014**)**, pp. 151-164.

44. B.J. Duggan, M. Hatherly, W.B. Hutchinson, P.T. Wakefield, Deformation structures and textures in cold-rolled 70: 30 brass, Met. Sci., **12** (1978), pp. 343-351.

45. K. Morii, H. Mecking, Y. Nakayama, Development of shear bands in fcc single crystals, Acta Metall., **33** (1985), pp. 379-386.

46. W. Hutchinson, B. Duggan, M. Hatherly, Development of deformation texture and microstructure in cold-rolled Cu–30Zn, Met. Technol., **6** (1979), pp. 398-403.

47. A.A. Saleh, E.V. Pereloma, A.A. Gazder, Texture evolution of cold rolled and annealed Fe–24Mn–3Al–2Si–1Ni–0.06 C TWIP steel, Mat. Sci. Eng. A, **528** (2011), pp. 4537-4549.

48. B.C. De Cooman, J. Kim, S. Lee, Heterogeneous deformation in twinning-induced plasticity steel, Scr. Mater., **66** (2012), pp. 986-991.

49. Y. Dastur, W. Leslie, Mechanism of work hardening in Hadfield manganese steel, Metall. Mater. Trans. A, **12** (1981), pp. 749-759.

50. P. Adler, G. Olson, W. Owen, Strain hardening of Hadfield manganese steel, Metall, Mater. Trans. A., **17** (1986), pp. 1725-1737.

51. L. Kubin, Y. Estrin, Dynamic strain ageing and the mechanical response of alloys, J. Phys. III, **1** (1991), pp. 929-943.

52. T. Shun, C. Wan, J. Byrne, A study of work hardening in austenitic Fe-Mn-C and Fe-Mn-Al-C alloys, Acta Metall. Mater., **40** (1992), pp. 3407-3412.

53. B. Zuidema, D. Subramanyam, W. Leslie, The effect of aluminum on the work hardening and wear resistance of Hadfield manganese steel, Metall. Mater. Trans. A, **18** (1987), pp. 1629-1639.

54. I. Gutierrez-Urrutia, D. Raabe, Dislocation and twin substructure evolution during strain hardening of an Fe–22wt.% Mn–0.6 wt.% C TWIP steel observed by electron channeling contrast imaging, Acta Mater., **59** (2011), pp. 6449-6462.

55. L. Lu, Y. Shen, X. Chen, L. Qian, K. Lu, Ultrahigh strength and high electrical conductivity in copper, Science, **304** (2004), pp. 422-426.

56. J.-E. Jin, Y.-K. Lee, Strain hardening behavior of a Fe–18Mn–0.6C–1.5Al TWIP steel, Mater. Sci. Eng. A, **527** (2009), pp. 157-161.



Fig. 1: XRD plots of (a) Initial material, (b) 20%, (c) 40% and (d) 60% cold rolled for steel-1, steel-2 and steel-3 samples.

Fig. 2: (111) pole figures depicting the initial texture for (a) Steel -1, (b) Steel -2 and (c) Steel-3 samples.

Fig. 3: $\Phi_2$ =0° , 45° and 65° sections of the ODF for (a) 40% cold rolled and (b) 60% cold rolled samples for Steel-1 to 3.

Fig. 4: Fibre plots for 40% deformed samples for Steel-1 to 3 (a) α-fibre, (b) β-fibre and (c) τ-fibre.

Fig. 5: Fiber plots for 60% deformed samples for Steel-1 to 3, (a) α-fibre, (b) β-fibre and (c) τ-fibre.

**Fig. 6:** $\Phi_2$ =0°, 45° and 65° sections of ODF for 60% deformed simulated texture for Steel-1 to 3.

**Fig. 7:** (a) Activity plot of slip and twin systems; (b) Twin volume fraction incorporated during texture simulation using PTR scheme.



Fig. 8: Starting microstructures for (a) Steel-1, (b) Steel-2 and (c) Steel-3 samples.

Fig. 9: Microstructures of 20% cold rolled sample for (a) Steel-1, (b) Steel-2 and (c) Steel-3.

Fig. 10: Microstructure of 40% cold rolled sample for (a) Steel-1, (b) Steel-2 and (c) Steel-3, showing the bundles of deformation twins.

Fig. 11: True stress and true strain plot for Steel-1, Steel-2 and Steel-3 samples. Inset shows the enlarge part of stress-strain curve showing frequency of serration.

Fig. 12: Twin boundary fraction with strain for Steel-1, Steel-2 and Steel-3. The tolerance angle was given 5° for twin fraction calculation.

Fig. 13: Misorientation distribution plots (0 - 65°) (a) 0%, (b) 20% and (c) 40% rolled samples. Misorientation at ~60° indicates the twin formation.

**Fig. 14:** Kernel average misorientation (KAM) plots (a) 0%, (b) 20% and (c) 40% cold rolled samples.

**Fig. 15:** Microstructure of 60% cold rolled sample for Steel-3 (Ni added), microstructure shows macroscopic shear bands (SBs) throughout the sample.



Fig. 16: Evolution of twin volume fraction with increasing tensile strain.

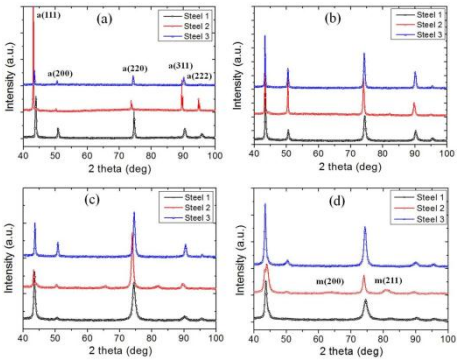


**Fig. 1:** XRD plots of (a) Initial material, (b) 20%, (c) 40% and (d) 60% cold rolled for Steel-1, Steel-2 and Steel-3 samples.

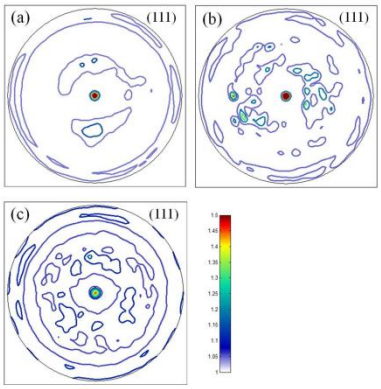


**Fig. 2:** (111) pole figures depicting the initial texture for (a) Steel -1, (b) Steel -2 and (c) Steel-3 samples.

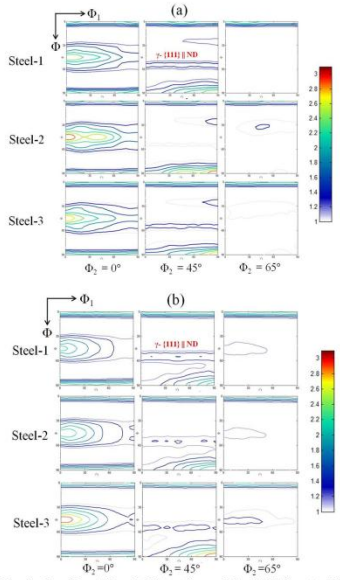


**Fig. 3:** $\Phi_2$=0° , 45° and 65° sections of the ODF for (a) 40% cold rolled and (b) 60% cold rolled samples for Steel-1 to 3.

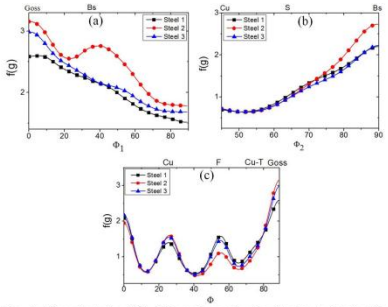


**Fig. 4:** Fibre plots for 40% deformed samples for Steel-1 to 3 (a) α-fibre, (b) β-fibre and (c) τ-fibre.

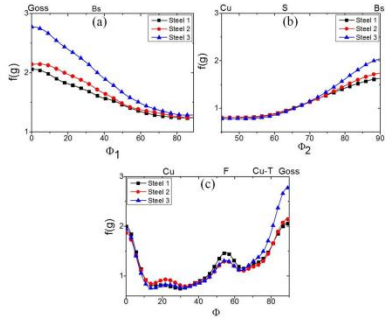


**Fig. 5:** Fiber plots for 60% deformed samples for Steel-1 to 3, (a) α-fibre, (b) β-fibre and (c) τ-fibre.

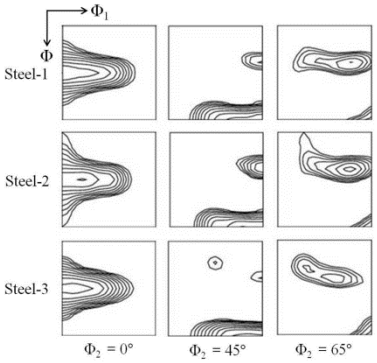


**Fig. 6:** $\Phi_2$ =0°, 45° and 65° sections of ODF for 60% deformed simulated texture for Steel-1 to 3.

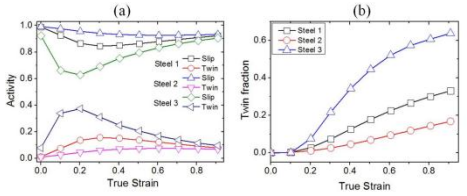


**Fig. 7:** (a) Activity plot of slip and twin systems; (b) Twin volume fraction incorporated during texture simulation using PTR scheme.

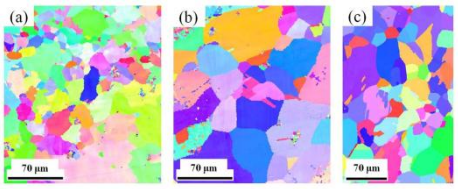


**Fig. 8:** Starting microstructures for (a) Steel-1, (b) Steel-2 and (c) Steel-3 samples.

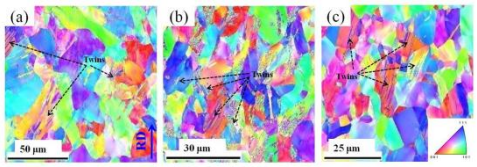


**Fig. 9:** Microstructures of 20% cold rolled sample for (a) Steel-1, (b) Steel-2 and (c) Steel-3.

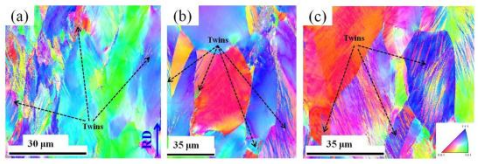


**Fig. 10:** Microstructure of 40% cold rolled sample for (a) Steel-1, (b) Steel-2 and (c) Steel-3, showing the bundles of deformation twins.

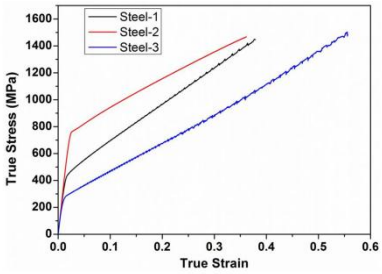


**Fig. 11:** True stress and true strain plot for Steel-1, Steel-2 and Steel-3 samples. Inset shows the enlarge part of stress-strain curve showing frequency of serration.

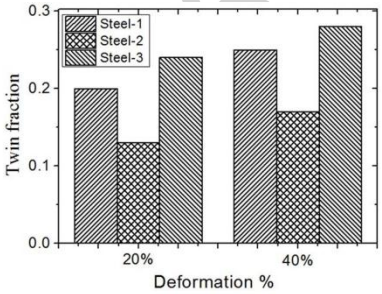


**Fig. 12:** Twin boundary fraction with strain for Steel-1, Steel-2 and Steel-3. The tolerance angle was given 5° for twin fraction calculation.

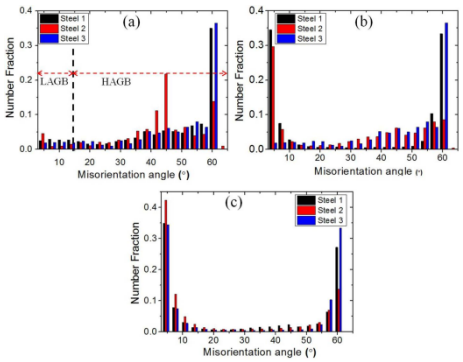


**Fig. 13:** Misorientation distribution plots (0 - 65°) (a) 0%, (b) 20% and (c) 40% rolled samples. Misorientation at ~60° indicates the twin formation.

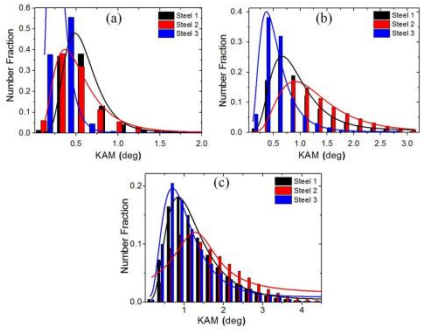


**Fig. 14:** Kernel average misorientation (KAM) plots (a) 0%, (b) 20% and (c) 40% cold rolled samples.

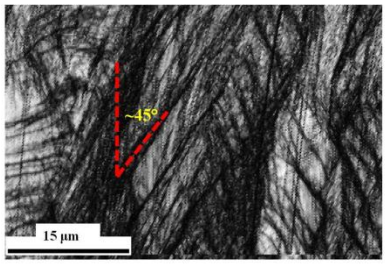


**Fig. 15:** Microstructure of 60% cold rolled sample for Steel-3 (Ni added), microstructure shows macroscopic shear bands (SBs) throughout the sample.

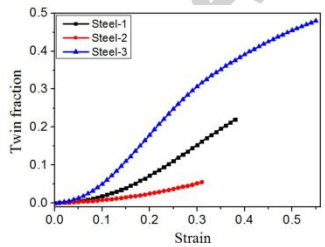


**Fig. 16:** Evolution of twin volume fraction with increasing tensile strain.

**Table 1:** Tested materials and their chemical composition

| Sample Name | Composition (wt. %) |
|---|---|
| Steel -1 | Fe-12.5Mn-0.52C |
| Steel-2 | Fe-12.1Mn-0.55C-3.6Al |
| Steel-3 | Fe-12.3Mn-0.53C -4.8Ni |

**Table 2:** Cold rolling reduction levels and the corresponding true strains

| Reduction (%) | 20 | 40 | 60 |
|---|---|---|---|
| True Strain ($\varepsilon_t$) | 0.22 | 0.51 | 0.92 |



**Table 3:** Some important FCC texture components and there corresponding Euler angles (Bunge notation)

| Texture Components {hkl}<uvw> | | Euler Angle $\Phi_1$, $\Phi$, $\Phi_2$ |
|---|---|---|
| Cu | {112}<111> | 90°, 35°, 45° |
| Goss | {110}<001> | 00°, 45°, 00° |
| Bs | {110}<112> | 35°, 45°, 00° |
| S | {123}<634> | 59°, 29°, 63° |
| Cu-T | {552}<115> | 90°, 74°, 45° |
| F | {111}<112> | 30°/90°, 55°,45° |

**Table 4:** Starting and ending Euler angles of α, β and τ fiber

| | Start Euler angle | End Euler angle | common axis of orientation |
|---|---|---|---|
| α-fiber | 00°, 45°, 00° | 90°, 45°,00° | <110>\|\|ND |
| β-fiber | 90°, 35°,45° | 35°,45°,90° | None |
| τ-fiber | 90°, 00°, 45° | 90°,90°,45° | <110>\|\|TD |



**Table 5:** Critical Resolved Shear Stress (CRSS) values for different slip and twin systems and imposed velocity gradient for rolling

| Sample Name | Slip/Twin systems | $\tau_0$ | $\tau_1$ | $\theta_0$ | $\theta_1$ | Imposed velocity gradient |
|---|---|---|---|---|---|---|
| Steel-1 | Slip | 30 | 40 | 60 | 10 | |
| | Twin | 45 | 50 | 30 | 15 | $\begin{bmatrix} 1 & 0 & 0 \\ 0 & 0 & 0 \\ 0 & 0 & -1 \end{bmatrix}$ |
| Steel-2 | Slip | 40 | 40 | 45 | 10 | |
| | Twin | 62 | 50 | 30 | 15 | |
| Steel-3 | Slip | 25 | 40 | 75 | 10 | |
| | Twin | 35 | 50 | 30 | 15 | |

**Table 6:** Yield strength (YS), ultimate tensile strength (UTS) and % elongation of steel-1 to 3

| | Yield strength (MPa) | Ultimate tensile strength (MPa) | Elongation (%) |
|---|---|---|---|
| Steel-1 | 410 ± 30 | 990 ± 50 | 46 ± 5 |
| Steel-2 | 760 ± 30 | 1468 ± 50 | 36 ± 5 |
| Steel-3 | 250 ± 30 | 852 ± 50 | 74 ± 5 |